Volume 12
Number 43
21 November 2024
Pages 11045–11268

Journal of Materials Chemistry B

Materials for biology and medicine

rsc.li/materials-b

ISSN 2050-750X

ROYAL SOCIETY OF CHEMISTRY

PAPER
Elisabet Gómez-González, Manuel Ocaña *et al.*
Sodium lanthanide tungstate-based nanoparticles as bimodal contrast agents for *in vivo* high-field MRI and CT imaging

Journal of
Materials Chemistry B

PAPER

View Article Online
View Journal | View Issue

Cite this: *J. Mater. Chem. B*, 2024, **12**, 11123

Sodium lanthanide tungstate-based nanoparticles as bimodal contrast agents for *in vivo* high-field MRI and CT imaging†

Elisabet Gómez-González, ‡*[a] Carlos Caro, ‡[bc] Nuria O. Núñez, [a]
Daniel González-Mancebo,[a] Jesús D. Urbano-Gámez,[bc]
Maria L. García-Martín [bcd] and Manuel Ocaña *[a]

Received 28th May 2024,
Accepted 20th August 2024

DOI: 10.1039/d4tb01157k

rsc.li/materials-b

Research on high-field magnetic resonance imaging (HF-MRI) has been increased in recent years, aiming to improve diagnosis accuracy by increasing the signal-to-noise ratio and hence image quality. Conventional contrast agents (CAs) have important limitations for HF-MRI, with the consequent need for the development of new CAs. Among them, the most promising alternatives are those based on Dy^{3+} or Ho^{3+} compounds. Notably, the high atomic number of lanthanide cations would bestow a high capability for X-ray attenuation to such Dy or Ho-based compounds, which would also allow them to be employed as CAs for X-ray computed tomography (CT). In this work, we have prepared uniform $NaDy(WO_4)_2$ and $NaHo(WO_4)_2$ nanoparticles (NPs), which were dispersible under conditions that mimic the physiological media and were nontoxic for cells, meeting the main requirements for their use *in vivo*. Both NPs exhibited satisfactory magnetic relaxivities at 9.4 T, thus making them a promising alternative to clinical CAs for HF-MRI. Furthermore, after their intravenous administration in tumor-bearing mice, both NPs exhibited significant accumulation inside the tumor at 24 h, attributable to passive targeting by the enhanced permeability and retention (EPR) effect. Therefore, our NPs are suitable for the detection of tumors through HF-MRI. Finally, $NaDy(WO_4)_2$ NPs showed a superior X-ray attenuation capability than iohexol (commercial CT CA), which, along with their high r_2 value, makes them suitable as the dual-probe for both HF-MRI and CT imaging, as demonstrated by *in vivo* experiments conducted using healthy mice.

1. Introduction

Imaging-based clinical diagnosis is pivotal in patient care.[1] Among the various imaging modalities available, magnetic resonance imaging (MRI) and computed tomography (CT) stand out for their ability to provide high-quality 3D anatomical and functional images, serving as invaluable tools for the non-invasive diagnosis of a large variety of diseases, being particularly relevant to their role in the battle against cancer through early diagnosis.[2]

The contrast in MRI images is due to the differences in the longitudinal (T_1) and transverse (T_2) relaxation times of the protons present in different tissues as well as in the proton content. T_1 shortening typically produces bright regions, while T_2 shortening typically produces dark regions. In some cases, contrast agents (CAs) that shorten the longitudinal (T_1) and transverse (T_2) relaxation times of the protons[3,4] are required to increase the contrast. The capability of a CA to shorten T_1 and T_2 is known as longitudinal (r_1) and transverse (r_2) relaxivities, respectively, which can be obtained as the slope of the line resulting from the plot of $1/T_{1,2}$ *vs.* CA concentration.

Although the conventional MRI technique is very well established in clinics, high-field MRI (HF-MRI) is being increasingly used in the field of preclinical imaging to improve the quality of the images since, as the magnetic field becomes stronger, the signal-to-noise ratio increases, leading to a higher resolution required to image small animals with sufficient details.[5] Additionally, high-field MRI systems are already a reality in

---

[a] *Instituto de Ciencia de Materiales de Sevilla (CSIC-US), c/Américo Vespucio, 49, 41092 Sevilla, Spain. E-mail: elisabet.gomez@icmse.csic.es, mjurado@icmse.csic.es*

[b] *Biomedical Magnetic Resonance Laboratory-BMRL, Andalusian Public Foundation Progress and Health-FPS, Seville, Spain*

[c] *Instituto de Investigación Biomédica de Málaga y Plataforma en Nanomedicina-IBIMA Plataforma Bionand, C/Severo Ochoa, 35, 29590 Malaga, Spain*

[d] *Biomedical Research Networking Center in Bioengineering, Biomaterials & Nanomedicine (CIBER-BBN), 28029 Madrid, Spain*

† Electronic supplementary information (ESI) available. See DOI: **https://doi.org/10.1039/d4tb01157k**

‡ Both authors contributed equally to this work.

clinical practice, with the approval of the first 7 T system by the Food and Drug Administration (FDA) in 2017.[6] Thus, while clinical scanners using 1.5 and 3 T magnets may achieve image resolutions of up to 1 mm, those using 7 T magnets have been shown to achieve resolutions as fine as 0.5 mm.[5,7] Another important advantage of using high fields is the decrease in image acquisition times.[8,9]

Unfortunately, most of the T_1-CAs, based on Gd^{3+} complexes or Gd-containing nanoparticles (NPs), and T_2-CAs, consisting of or superparamagnetic iron oxides (SPIONS), used for conventional MRI are less suitable for HF-MRI. In the first case, this is due to the decrease of the value of r_1 of Gd^{3+}-based CAs with the increasing applied magnetic field as a result of increasing electron spin longitudinal relaxation times with increasing field strength.[10,11] In the case of T_2-CAs, in agreement with the quantum mechanical theory of the outer sphere,[12–14] the value of r_2 should increase as increasing magnetization, and, hence, as the increasing magnetic field. For SPIONS, a saturation of their magnetization takes place at a low field (1 T), which is an important drawback for the use of these CAs in HF-MRI.[15,16] Therefore, the development of new CAs for HF-MRI is required; the best candidates being those based on lanthanide (Ln^{3+}) ions other than Gd^{3+}, such as Dy^{3+} and Ho^{3+}. These cations have short electronic relaxation times and the highest magnetic moments among all Ln^{3+} cations that prevent their magnetization from saturating as the magnetic field increases.[17] It is noteworthy that, because of the high atomic number of Ln^{3+} cations, the Dy or Ho-based MRI CAs should show a high capability for X-ray attenuation,[18] which would also allow them to be employed as CAs for X-ray computed tomography (CT).[19] The interest in such multifunctional probes has increased during the last few years because the combined use of more than one imaging technique is very convenient to obtain a more reliable diagnosis.[20]

Several reports can be found in the literature regarding Dy^{3+} or Ho^{3+} containing NPs for bimodal HF-MRI and CT imaging, most of them based on fluoride matrices,[21–24] which tend to dissolve in aqueous media,[25,26] leading to the release of fluoride ions that are potentially toxic,[27] although this drawback can be mitigated by surface functionalization.[28] As an alternative to fluorides, Dy^{3+} NPs based on other matrices, such as oxide,[29,30] phosphate,[31,32] vanadate,[33] or molybdate,[34] have been proposed. However, the potentiality of double sodium-dysprosium or holmium tungstate ($NaDy(WO_4)_2$ and $NaHo(WO_4)_2$) NPs as CAs for HF-MRI has not yet been addressed, despite the high atomic number of tungsten when compared with fluorine, vanadium, or phosphor, which would confer a higher X-ray attenuation capability to these probes.

Finally, it is widely accepted that, for *in vivo* applications, the NPs must be uniform with a size of ≤100 nm.[35] In addition, they must be colloidally stable in physiological media[36] and, obviously, must be biocompatible.[37] The later requirements are affected by several factors, such as the size, shape, and composition of the NPs,[38] which must be adjusted to optimize the performance of CAs.

It should also be noticed that intravenously administered nanoparticles preferentially accumulate in tumors due to their intrinsic physiology,[39] a phenomenon known as the enhanced permeability and retention (EPR) effect.[40] Extensively studied in nanotechnology, the EPR effect is widely regarded as the most efficient mechanism for targeting nanoparticles to solid tumors,[41,42] despite some existing controversies.[43,44]

In this work, we have developed a procedure for the synthesis of uniform and well-dispersed sodium dysprosium tungstate ($NaDy(WO_4)_2$) NPs with a quasi-spherical shape and more anisometric sodium holmium tungstate ($NaHo(WO_4)_2$) NPs, and both of them functionalized with polyacrylic acid (PAA). The colloidal behavior in several physiological media and the *in vitro* cytotoxicity of such NPs have been evaluated to assess their suitability for *in vivo* applications. Finally, the magnetic relaxivity at high field (9.4 T) and the X-ray attenuation properties of the developed CAs were comparatively analyzed, and their *in vivo* behavior (pharmacokinetic and biodistribution) after intravenous injection in tumor-bearing mice was evaluated by using HF-MRI and CT to explore their potentiality as dual contrast agents for both bioimaging techniques.

2. Experimental section

2.1. Reagents

Dysprosium nitrate pentahydrate ($Dy(NO_3)_3{\cdot}5H_2O$, Sigma Aldrich, 99.99%), holmium nitrate pentahydrate ($Ho(NO_3)_3{\cdot}5H_2O$, Sigma Aldrich, 99.99%), sodium tungstate dihydrate (Na_2WO_4, Sigma Aldrich, ≥99%), ethylene glycol (EG, Sigma Aldrich, 99.8%), and polyacrylic acid (PAA, Sigma Aldrich, Mw 1800) were used as received. A phosphate-buffered saline (PBS) solution (137 mM NaCl, 2.7 mM KCl and 10 mM phosphate, with pH = 7.4) was prepared by dissolving a PBS tablet (Sigma-Aldrich) in 200 mL of Milli-Q water. 2-(*N*-Morpholino)ethanesulfonic acid (MES) solution was prepared following the next protocol: 1.06 g of MES were dissolved in Milli-Q water, to obtain a 50 mM buffer, pH 6.5. Saline solution was used as received.

2.2. Nanoparticle synthesis

2.2.1. Sodium dysprosium tungstate. $NaDy(WO_4)_2$ NPs were prepared by employing a polyol-based method through homogeneous precipitation reactions. Essentially, the method involves the aging, in a microwave-assisted oven at 220 °C for 1 h, of a dysprosium nitrate and sodium tungstate solution in a mixture of EG and water (volume ratio = 4/1). For this, sodium tungstate was first dissolved under magnetic stirring in 5 mL of EG at ∼80 °C and then, it was cooled down to room temperature. In another vial, dysprosium nitrate was dissolved along with 2 mg mL^{-1} PAA in 2 mL of Milli-Q water. After this, 3 mL of EG were added. These two precursor solutions were admixed to obtain a solution with final concentrations 0.04 M $Dy(NO_3)_3$ and 0.1 M Na_2WO_4. Finally, the mixture was homogenized and aged for 1 hour in a microwave-assisted oven at 220 °C.

2.2.2. Sodium holmium tungstate. $NaHo(WO_4)_2$ NPs were synthesized by using the protocol described above, introducing slight modifications to obtain uniform NPs. Specifically, 0.02 M holmium nitrate was employed instead of 0.04 M dysprosium nitrate as Ln^{3+} precursor.

For purification, the resulting dispersions were cooled down and centrifuged to remove the supernatants. The NPs were then washed twice with ethanol and once with double distilled water.

Finally, the particles were stored dispersed in double-distilled water or dried at 50 °C, when required.

2.3. Characterization techniques

A JEOL 2100 Plus (200 kV) transmission electron microscope (TEM) was employed to obtain micrographs of the NPs, from which size distribution histograms were obtained by counting about one hundred of particles on the TEM micrographs, using the free software ImageJ.

A Panalytical, X'Pert Pro diffractometer (CuKα) with an X-Celerator detector was used to record the X-ray diffraction (XRD) patterns ($10^\circ < 2\theta < 90^\circ$, a 2θ step width of 0.03°, and 10 s counting time).

The infrared spectra (FTIR) of the NPs dispersed in KBr pellets were recorded with a Jasco FT/IR-6200 Fourier transform spectrometer. A TA Instruments-TGA apparatus (SDT Q600) was employed to conduct the thermogravimetric analysis (TGA) in an air atmosphere at a heating rate of 10 °C min^{-1}.

The hydrodynamic diameter of the NPs in water, MES, PBS or saline solution dispersions (NPs content = 0.5 mg mL^{-1}) was evaluated by dynamic light scattering (DLS) using a Malvern Zetasizer Nano-ZS90 apparatus.

The transverse relaxation rate ($R_2 = 1/T_2$) was measured for aqueous suspensions of NPs with different concentrations of Ln^{3+} (0.062 to 0.5 mM) using a Bruker Biospec MRI system at 9.4 T, employing a Carl–Purcell–Meiboom–Gill (CPMG) imaging sequence. The transverse relaxivity, r_2, values were determined from the slope of the linear fit of the transverse relaxation rate ($R_2 = 1/T_2$) *vs.* Ln^{3+} concentration (mM).

The measurements of the magnetization behavior were performed at 300 K using a vibrating sample magnetometer (8600 Series VSM, Lake Shore Cryotronics, USA) and magnetic fields ranging from −19 000 to 19 000 Oe, with a sample concentration of 1 mg mL^{-1} of Ln^{3+}.

X-ray attenuation of aqueous NP dispersions or iohexol solutions having different CA concentrations (0, 5, 10, 15, and 20 mg mL^{-1}, total volume = 1.0 mL) were measured with a Zeiss Xradia 610 Versa 3D X-ray microscope (XRM) with 0.4× objective lens without any filter, achieving a pixel size of 213 μm. The fixed acquisition parameters were 123 μA current, 70 kVp voltage and 0.1 s of exposure time. The software called Reconstructor Scout and Scan 16.1.13.038 was utilized to reconstruct the final images from 801 projections. Finally, the resulting images were analyzed with ImageJ (a free-license software) using a spherical volume of 0.5 cm in radius. For image calibration, the intensity value of water X-ray attenuation was considered to be 0 Hounsfield units (HU), and the air attenuation was −1000 HU.

The NP concentration in all prepared dispersions was determined by ICP analyses performed using an iCAP 7200 ICP-OES Duo (ThermoFisher Scientific) equipment. The NPs were previously digested in concentrated hydrochloric acid at room temperature overnight.

2.4. Cell experiments

2.4.1. Cell culture. HFF-1 human fibroblast cells were used for the cytotoxicity assessment. They were cultured in the DMEM supplemented with L-glutamine (2 mM), FBS (10%), and penicillin/streptomycin (1%). 4T1, a triple-negative breast cancer cell line used to develop mice tumor models, was cultured in the RPMI growth medium supplemented with L-glutamine (2 mM), FBS (10%), and penicillin/streptomycin (1%). Both cell lines were maintained at 37 °C in a 5% CO_2 incubator.

2.4.2. Cytotoxicity assays. HFF-1 cells were cultured in the presence of NPs ($\leq$100 μg mL^{-1} of Ln^{3+}) to evaluate the cell viability through MTT and live–dead assays, following the protocols described elsewhere.[31]

2.5. *In vivo* experiments

2.5.1. Animal handling. *In vivo* assays were performed following the ethical guidelines of both national and European regulations for the care and use of laboratory animals (R.D. 53/2013 and 2010/62/UE) and approved by our local Animal Research Ethics Committee (Comité de Etica de Experimentación Animal (CEEA) IBIMA-Plataforma BIONAND) and the Highest Institutional Ethical Committee (Andalusian Government, accreditation number 14/09/2021/130). Before MRI and CT experiments, animals were anesthetized with isoflurane 3% (1–1.5 mL min^{-1}), and the tail vein was cannulated for the intravenous injection of NP suspensions. Then, the animals were positioned in the imaging system, where they remained anesthetized by receiving a 1% isoflurane flow of 1 mL min^{-1}, and their respiration rate and temperature were monitored.

2.5.2. Tumor implantation. Orthotopic breast tumors were induced by 4T1 cell implantation into the mammary tissue, as previously described.[45]

2.5.3. Pharmacokinetics and biodistribution. HF-MRI was employed to determine the pharmacokinetics and biodistribution of the developed NPs. For this, an aliquot of NPs suspended in PBS corresponding to 5 mg of Ln^{3+} (∼20 mg NPs) per kg animal was administered to tumor-bearing mice (n = 3, 22–25 g of weight), provided by Charles River, and the HF-MRI images were obtained using a 9.4 T Bruker Biospec system mentioned above and following the protocols described elsewhere.[46] Details on the acquisition scheme are provided in the ESI.†

2.5.4. *In vivo* bimodal HF-MRI and CT imaging. For these experiments, we followed a procedure similar to that described above for the biodistribution assays, except that we used healthy mice to which a higher concentration of the CA (10 mg Ln^{3+} (∼40 mg NPs) per kg animal) was administrated to reach concentrations detectable by CT scanning. Notably, while the concentration of CA was higher than that used in MRI experiments, it still remained significantly lower than the concentrations of iohexol typically used in clinical studies.[47] For CT imaging, we followed the protocols outlined in our previous publications,[48] using a Bruker Albira system (Bruker Biospec, Bruker BioSpin, Ettlingen, Germany), and the following parameters: 35 μm X-ray focal spot size (nominal), 45 kVp energy, working at 400 μA. Attenuation values were expressed in Hounsfield units, with the scale adjusted to better visualize soft tissues, overexposing the bones.

2.6. Statistical analysis

The statistical analysis was performed using the Jamovi software 2.3.21. The Mann–Whitney *U* test was selected for cell viability, *in vivo* T_2, and ICP values, which are displayed as mean ± standard deviation (SD).

2.7. Histology

After *in vivo* experiments, animals were euthanized, and tissue samples from the liver and tumor were harvested. These samples were processed and stained with hematoxylin and eosin (H&E) before their histological examination by light microscopy. Detailed protocols can be found in the ESI.†

3. Results and discussion

3.1. Nanoparticle synthesis and characterization

The NPs obtained for the Dy^{3+}-based system showed an almost equiaxed shape (Fig. 1a) and a mean size of 17 nm with a rather narrow size distribution (standard deviation, $\sigma = 4$) (Fig. 1b), whereas those corresponding to the Ho-based system were more anisometric (Fig. 1c) and slightly smaller (19 nm ($\sigma = 4$) × 8 nm ($\sigma = 1$)) (Fig. 1d). These morphological differences may be explained based on the differences in the precursor concentration used for the synthesis of both systems and by the probable small different reactivity of both lanthanide cations, since, according to the well-known LaMer and Dinegar model,[49] these factors determine the precipitation kinetics and hence the particle size and shape.

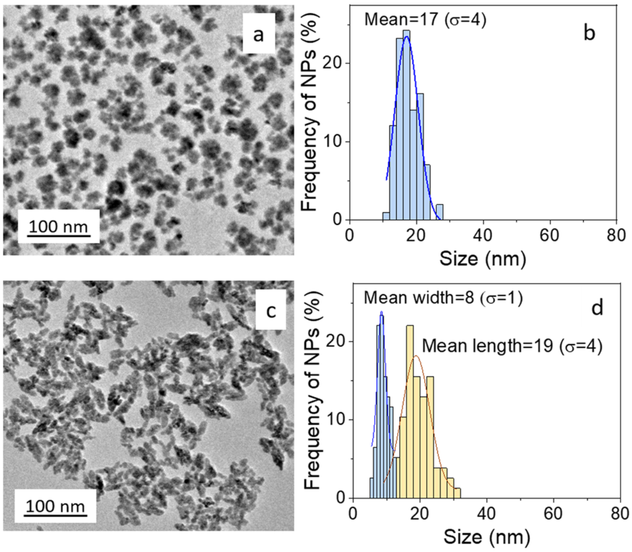

Fig. 1 TEM micrographs and particle size histograms of the dysprosium (a) and (b) and holmium (c) and (d) tungstate-based systems.

According to XRD, both types of NPs (Fig. 2a) crystallized into the tetragonal structure since their corresponding pattern was very similar, exhibiting a set of reflections compatible with the PDF file for tetragonal $NaDy(WO_4)_2$ (PDF: 96-222-4801). The FTIR spectra of these samples (Fig. 2b) were also very similar and displayed the lattice vibrations modes ($<1000\ cm^{-1}$) expected for the tetragonal $NaLn(WO_4)_2$ phases,[50] along with two bands at 3400 and 1625 cm^{-1}, respectively, due to adsorbed water. More interestingly, some absorptions between 1400 and 1550 cm^{-1} were also observed, which correspond to the symmetric and asymmetric stretching vibrational modes of the PAA carboxylate anions, respectively,[51] indicating the incorporation of PAA molecules onto the NP surface. The amount of such molecules was quantified from the TG curve (Fig. 2c) obtained for these NPs, which showed a first weight loss (3.5% for $NaDy(WO_4)_2$ and 2.5% for $NaHo(WO_4)_2$) below 300 °C, due to the release of adsorbed water, and a second one from 300 to 600 °C of ∼4.5% for both samples that can be related to the PAA decomposition.

3.2. Dispersibility in physiological media

The hydrodynamic diameter (HD) in aqueous suspensions obtained by DLS for both systems (Fig. 3) was similar and was kept within the nanometer size range (60 nm for $NaDy(WO_4)_2$ NPs and 57 nm for $NaHo(WO_4)_2$ NPs). This finding indicates that the NPs were not significantly aggregated in water. More interestingly, also in both cases, the HDs for the NPs dispersed in different media simulating physiological conditions, such as MES, PBS, and saline solution, were below 100 nm with PDI values of <0.2 in all cases, which correspond to moderately monodispersed particles. This finding indicates that our NPs meet the dispersibility requirement for their *in vivo* applications. It should be noticed that the HD in PBS of NPs synthesized using a similar procedure but in the absence of PAA was much higher (>700 nm) (Fig. S1, ESI†), which revealed the important role of PAA functionalization on the colloidal stability of our NPs required for *in vivo* applications.

3.3. Cell viability

The cell viability analyses were performed using the HFF-1 cell line as a working model, aiming to evaluate the potential cytotoxicity of the $NaDy(WO_4)_2$ and $NaHo(WO_4)_2$ NPs. This study relied on two procedures: (i) the live–dead assay, which provides information about changes in the cell morphology and the induction of necrotic and apoptotic processes, and (ii) the MTT assay, which assesses the mitochondrial activity of the cells.

By merging bright field microscopy images with fluorescence images of DAPI (blue, live cells) and TO-PRO-3 (red, dead cells) staining (Fig. 4a–d), it was observed that when the cells were exposed to NP concentrations of up to 100 μg mL^{-1}, referred to Dy^{3+} (Fig. 4c) or Ho^{3+} cations (Fig. 4d), no remarkable morphological changes with respect to death negative control were detected (Fig. 4a). We also found that there was no statistically significant ($p < 0.05$) decrease for any of the assayed concentrations (≤100 μg mL^{-1}) when counting the

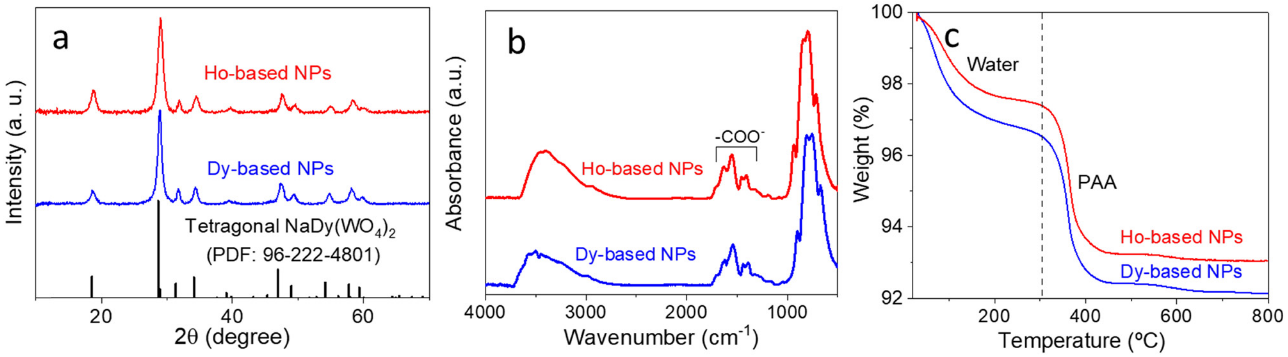

Fig. 2 XRD patterns (a), FTIR spectra (b), and TGA curves (c) of the $NaDy(WO_4)_2$ and $NaHo(WO_4)_2$ NPs.

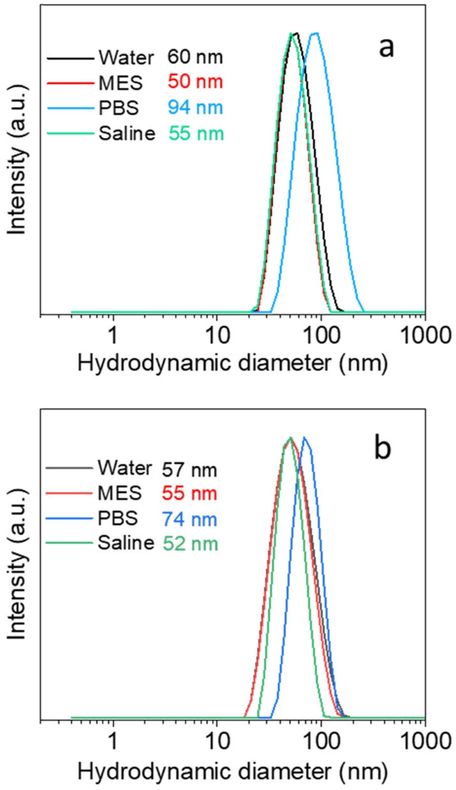

Fig. 3 DLS curves obtained for the $NaDy(WO_4)_2$ (a) and $NaHo(WO_4)_2$ (b) NPs dispersed in water, MES, PBS and saline solution.

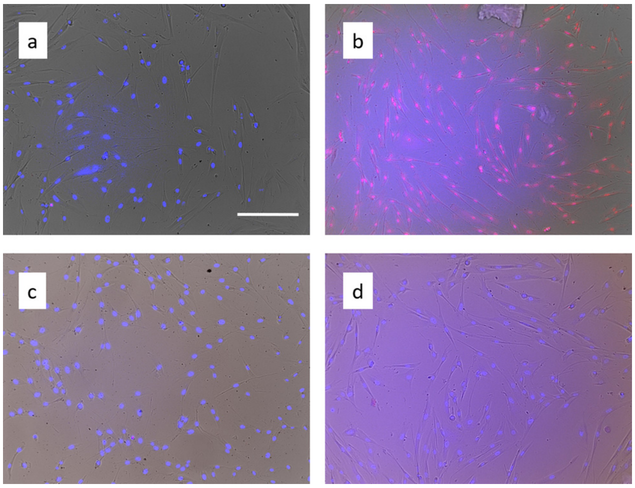

Fig. 4 Representative optical microscopy images of HFF-1 fibroblasts resulting from the merge of bright field (grey), DAPI (blue) and TO-PRO-3 iodine (red) images: (a) negative control, (b) positive control, (c) cells exposed to 100 μg mL^{-1} Dy of $NaDy(WO_4)_2$, and (d) cells exposed to 100 μg mL^{-1} Ho of $NaHo(WO_4)_2$. The scale bar corresponds to 50 μm.

total number of cells per well for both the $NaDy(WO_4)_2$ (Fig. 5a) and the $NaHo(WO_4)_2$ samples (Fig. 5d). This behavior is indicative of the absence of cell necrosis. On the other hand, no statistically significant differences ($p < 0.05$) were observed between the percentage of dead cells when exposed to the Ln concentrations up to ≤ 100 μg mL^{-1} and that corresponding to the negative control, indicating the absence of apoptosis for both samples (Fig. 5b and e).

Finally, the MTT assay showed no statistically significant effect on mitochondrial activity for both $NaDy(WO_4)_2$ and $NaHo(WO_4)_2$ samples (Fig. 5c and f), as the cell survival was above the limit below which (70%) NPs are considered to be potentially cytotoxic (UNE-EN ISO 10993-5:2009 standard).[52] Therefore, it can be concluded that the cell viability of the developed $NaDy(WO_4)_2$ and $NaHo(WO_4)_2$ NPs functionalized with PAA was very high and, therefore, they would be suitable for use as probes in bioimaging applications.

3.4. High-field magnetic resonance imaging

3.4.1. Relaxivity properties. The relaxivity values of the developed bioprobes were estimated *in vitro*, before the evaluation of their *in vivo* performance. The T_2-weighted MRI phantom images obtained at 9.4 T for the $NaDy(WO_4)_2$ and $NaHo(WO_4)_2$ NPs functionalized with PAA (Fig. 6, top) darkened as the increasing concentration of both kinds of NPs in the aqueous suspensions, which indicates that they behave as negative CAs. This was confirmed by measuring the r_1 (Fig. S2, ESI†) and r_2 (Fig. 6, down) values from the slope of the line resulting when plotting $1/T_{1\,\mathrm{or}\,2}$ *versus* lanthanide concentrations. As shown in these figures, for both systems, the r_2 value was much higher (105.6 and 58.6 mM^{-1} s^{-1}, for $NaDy(WO_4)_2$

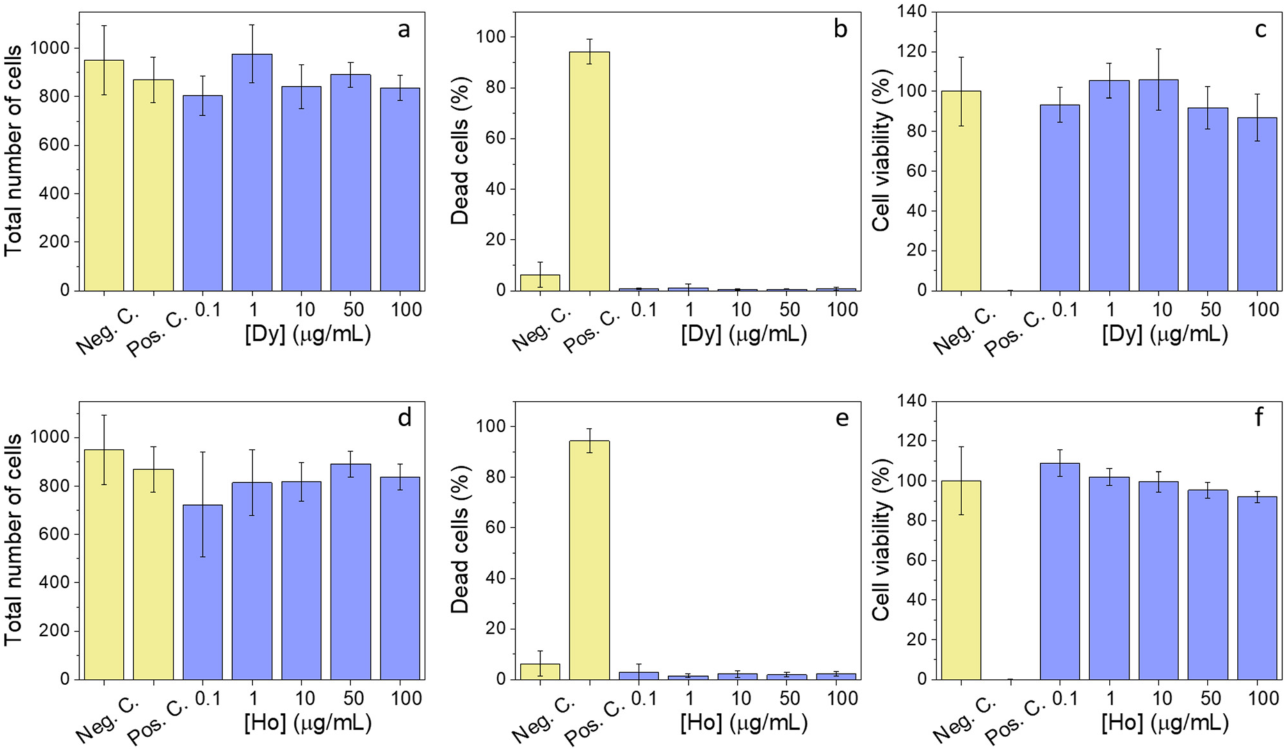

Fig. 5 Total number of cells per well after exposure for 24 h to increasing concentrations of $NaDy(WO_4)_2$ (a) and $NaHo(WO_4)_2$ (d) NPs. Percentage of dead cells after exposure to increasing concentrations of $NaDy(WO_4)_2$ (b) and $NaHo(WO_4)_2$ (e) NPs. The MTT assay for cells exposed for 24 h to increase concentrations of $NaDy(WO_4)_2$ (c) and $NaHo(WO_4)_2$ (f) NPs.

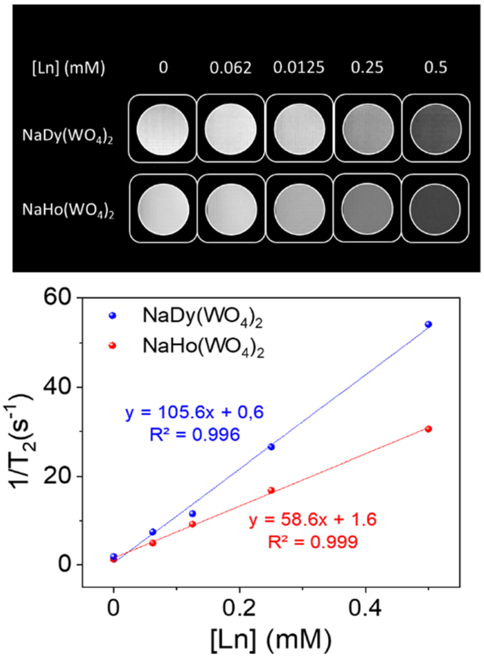

Fig. 6 T_2-weighted phantom images (top) and relaxation rates ($1/T_2$) *vs.* Ln concentrations (down) obtained at 9.4 T for aqueous suspensions of $NaDy(WO_4)_2$ (blue) and $NaHo(WO_4)_2$ (red) NPs.

and $NaHo(WO_4)_2$, respectively) than the r_1 value (0.29 and 0.27 mM^{-1} s^{-1}, for $NaDy(WO_4)_2$ and $NaHo(WO_4)_2$, respectively), which results in r_2/r_1 ratios (364 and 217, respectively) exceedingly above the lower limit ($\sim$10) for a system to be considered as T_2 CA.[3] It is also outstanding that the r_2 value was higher for the Dy-based NPs (105.6 mM^{-1} s^{-1}) than that for the Ho-based ones (58.6 mM^{-1} s^{-1}), which manifests the better performance of the former as a CA for HF-MRI. To explain this behavior, it must be considered that the value of the transverse relaxivity, r_2, of paramagnetic NPs is mainly due to the contribution of the Curie effect to the transverse relaxivity in the outer-sphere regime according to the quantum-mechanical theory.[12] Different factors influence the magnetization of paramagnetic Dy^{3+}- and Ho^{3+}-containing samples, such as the magnetic moment of such cations. Specifically, the r_2 value increases with the magnetization of the paramagnetic ion, which is related to the magnetic susceptibility and thus to the magnetic moment of the ion according to Curie's law, which predicts that the magnetization increases quadratically with the magnetic moment.[21] Therefore, since the value of the magnetic moment is higher for Dy^{3+} ($10.63\mu_B$) than for Ho^{3+} ($10.6\mu_B$),[53] the magnetization of the Dy-based system is also higher than that of the Ho-based one (Fig. S3, ESI†), thus explaining the higher r_2 value of the former. Another factor contributing to such a higher r_2 value is the higher particle size of the Dy-based sample since the quantum-mechanical theory[12] also predicts that r_2 increases with the particle size. Finally, it is important to mention that, as observed in in Table S1 (ESI†), the r_2 values of our samples are within the range reported for most of the other Dy or Ho based systems.[22–24,29–34,54,55] Only those based on LnF_3,[22] $LnVO_4$,[33] and

$LnPO_4$,[31,32] (Ln = Ho or Dy) previously reported by us showed clearly higher r_2 values due to their higher particle size. However, in these cases, the suitability of developed NPs as CAs for *in vivo* dual MRI-CT imaging was not investigated.

3.4.2. Pharmacokinetic and biodistribution in tumor-bearing mice. The *in vivo* behavior of the developed CAs was evaluated by HF-MRI following their intravenous administration (5 mg Ln^{3+} per kg animal) in tumor-bearing mice using 4T1 breast cancer as the tumor model. The aim was to determine the tumor-targeting capabilities of these new NPs *via* the EPR effect. Short-term and long-term pharmacokinetics were evaluated by dynamic T_2-weighted MRI quantitative T_2 mapping, respectively. It was observed that $NaDy(WO_4)_2$ NPs were rapidly removed from the bloodstream by the liver, leading to ~80% absolute relative enhancement (RE) increase within a few seconds (Fig. 7a). In contrast, $NaHo(WO_4)_2$ NPs exhibited a slower uptake, with RE variations ranging from ~60% at the beginning of the experiment to ~80% after 30 min (Fig. 7a). The lower uptake of the latter is probably due to their smaller HD since the nature of the coating is similar in both cases. On the other hand, the spleen displayed a gradual uptake over time, with this effect being more prominent for $NaDy(WO_4)_2$ NPs (Fig. 7b). The mild discrepancies noted for the liver and spleen can be explained (partially or fully) by the differing affinities for nanomaterials of Kupffer cells and splenic macrophages.[56] It should be noticed that there were no observed changes in either the tumor or the muscle during these first 30 minutes (Fig. S4, ESI†). Regarding long-term pharmacokinetics, high-resolution T_2-weighted images and parametric T_2 images were acquired at 1 and 24 hours following the administration of either $NaDy(WO_4)_2$ or $NaHo(WO_4)_2$ NPs. T_2-weighted images evidenced a sharp darkening in both the liver and the spleen at 1 hour, which was still evident at 24 hours (Fig. 7c). Although no changes were observed in the tumor for either of the NPs at 1 hour post-administration, at 24 hours, a noticeable darkening could be clearly observed, forming a ring around the necrotic zone (Fig. 7c). These findings are in agreement with previous reports that identified 24 hours as the optimal timeframe for passive tumor targeting by the EPR effect.[4,57,58] Interestingly, the accumulation behavior described in this work resembles the findings reported recently by some of us, where we identified the accumulation zone as distinct from the extravasation pattern delineated by Gd complexones.[45] Finally, as expected, no changes were detected in the muscle.[48] In addition, the quantitative T_2 mapping evaluation of the tumor revealed a statistically significant ($p < 0.05$) ΔR_2 in the accumulation zone for both NPs (approximately 2 s^{-1} for $NaDy(WO_4)_2$ and 7 s^{-1} for $NaHo(WO_4)_2$) (Fig. 7d). The accurate T_2 quantification of the liver and spleen was hindered by the remarkably high transverse relaxivity of our NPs, which led to extremely low T_2 values. However, the accurate estimation of NP accumulation could be obtained post-mortem by ICP analysis of the main organs (Fig. 7e). The majority of NPs were taken up by the liver and spleen, approximately 50% for $NaDy(WO_4)_2$ NPs and 25% for $NaHo(WO_4)_2$ NPs, with these differences showing a trend towards significance ($p < 0.1$) in both organs. Regarding tumor targeting, the percentage relative to the injected dose was below 1%, indicating a poor EPR effect, yet similar to those reported in the literature for most NPs.[59] However, this low amount proved sufficient for clear detection by MRI using both kinds NPs, in spite of their different values of r_2.

3.4.3. *Ex vivo* histological evaluation of tumor-bearing mice after intravenous administration. Histological evaluation of the liver and tumor was conducted at the end of the experiments, *i.e.*, 24 h after the intravenous administration of $NaDy(WO_4)_2$ and $NaHo(WO_4)_2$ NPs. For this purpose, sections of both tissues were stained with H&E. It was found (Fig. 8) that the tumor sections exhibited a heterogeneous cytoarchitecture and the characteristic high cell density of solid tumors. Furthermore, metastatic tumor granulocytes were clearly observed in the liver of tumor-bearing mice, as expected for this well-known metastatic tumor model, and consistent with previous studies conducted by some of us.[60] Notably, no acute tissue damage attributable to NP exposure was observed in any of the organs evaluated by histopathological analysis, further supporting the suitability of the herein-reported NPs for *in vivo* applications.

3.5. Dual HF-MRI-CT bioimaging

To explore the dual character of the developed NPs for HF-MRI and CT bioimaging, the $NaDy(WO_4)_2$ system was chosen, as a proof of concept, owing to their superior r_2 values when compared with the Ho-based system. For such a purpose, the X-ray attenuation properties of the selected sample were first evaluated.

3.5.1. X-ray attenuation properties. The X-ray attenuation properties of the $NaDy(WO_4)_2$ sample were measured for aqueous suspensions containing different NP concentrations. The X-ray attenuation phantom images obtained for these NP suspensions compared with those of iohexol (a commercial iodine-based CT contrast agent) are shown in Fig. 9 (top). From these images, it follows that for each concentration, the $NaDy(WO_4)_2$ NPs gave rise to a higher contrast than iohexol. This behavior can be quantified by plotting the X-ray attenuation values in Hounsfield units (HU) *vs.* the NP concentration (Fig. 9, bottom). As expected, the HU values increased linearly with the CA concentration. More interestingly, the slope of the best-fit line corresponding to the $NaDy(WO_4)_2$ NPs (31.6 HU per mg mL^{-1}) was much elevated than that obtained for iohexol (18.8 HU per mg mL^{-1}) evidencing that a lower dose of the $NaDy(WO_4)_2$-based CA is needed to produce a similar contrast, which would be advantageous for the patients. The better X-ray attenuation capacity of our CA is explained by the higher atomic number of dysprosium (Z = 66) and mainly tungsten (Z = 74), in comparison with that of iodine (Z = 53), since the X-ray attenuation coefficient increases with the fourth power of Z.[61]

3.5.2. *In vivo* dual HF-MRI-CT bioimaging. The $NaDy(WO_4)_2$ NPs were intravenously administrated in healthy mice using a higher dose (10 mg Dy per kg animal) than the one used for pharmacokinetic and biodistribution studies since CT is less sensitive than HF-MRI. The HF-MRI and CT images recorded for the same injected mouse (Fig. 10) showed a clear contrast in the liver and spleen 1 h after administration, which did not change

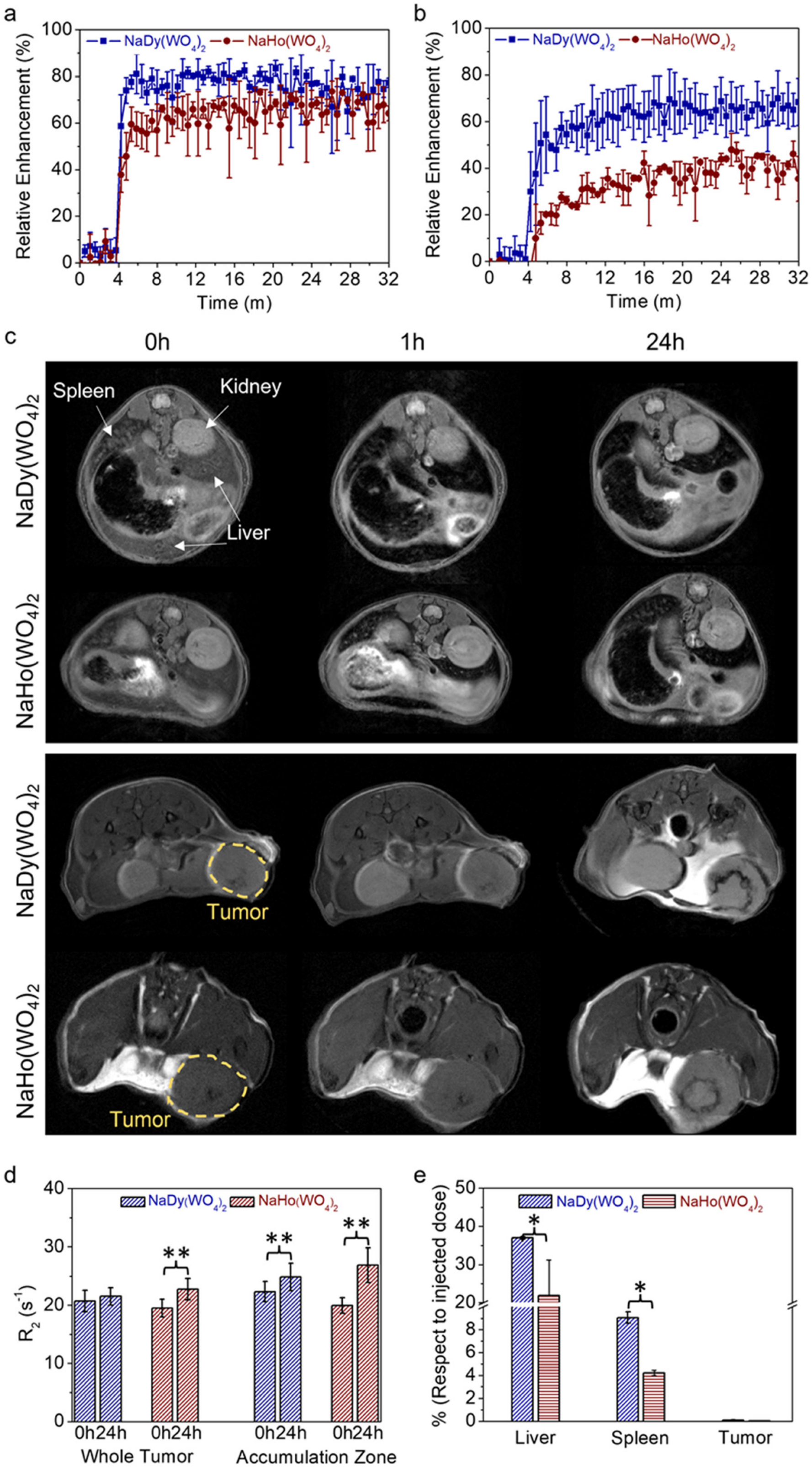

Fig. 7 *In vivo* pharmacokinetics of the liver (a) and spleen (b) after the intravenous administration in tumor-bearing mice of DyW (blue) or HoW (red). Representative T_2-weighted MR images at 0, 1 and 24 hours after the intravenous injection of NPs (c). ΔR_2 values of tumor (whole and tumor periphery) (d). Relative Dy and Ho concentrations (% to the injected dose) (e). The average values were obtained by performing three experiments. The statistical test was significant for data with * ($p < 0.1$) and ** ($p < 0.05$).

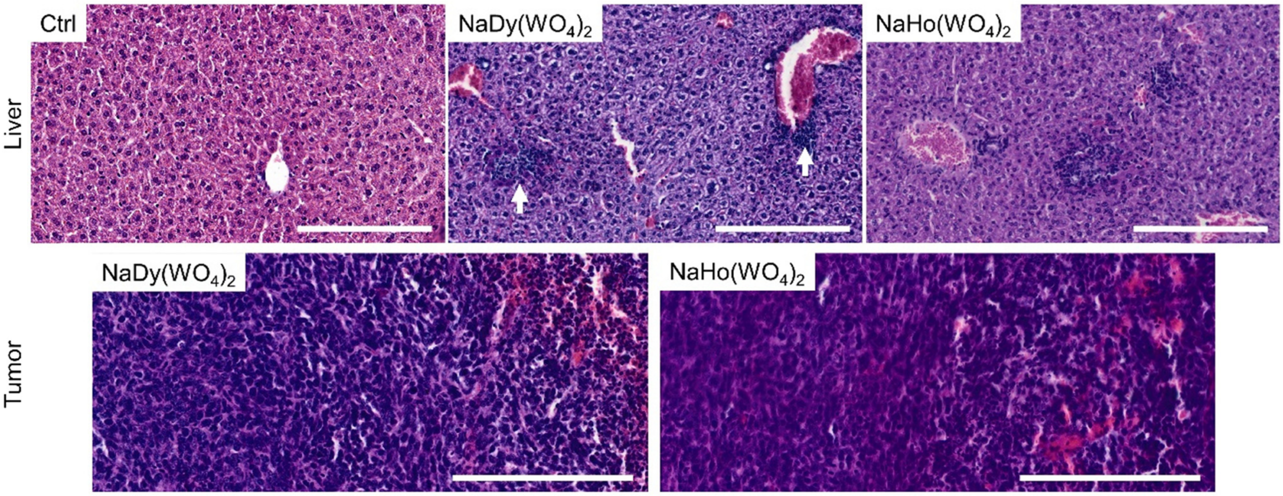

Fig. 8 Representative histological sections of H&E staining of the liver (top) and tumor (bottom) of 4T1 tumor-bearing mice at 24 hours post-intravenous administration of NPs. The liver of non-tumor-bearing mice was used as controls (Ctrl). Arrows indicate metastatic lesions. The scale bar corresponds to 200 μm.

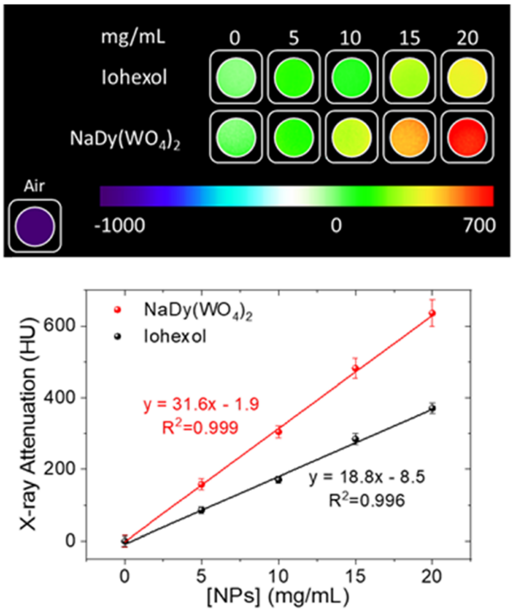

Fig. 9 X-ray attenuation phantom images (top) and X-ray attenuation values in Hounsfield units (HU) (bottom) obtained for aqueous suspensions having different concentrations of $NaDy(WO_4)_2$ NPs and iohexol.

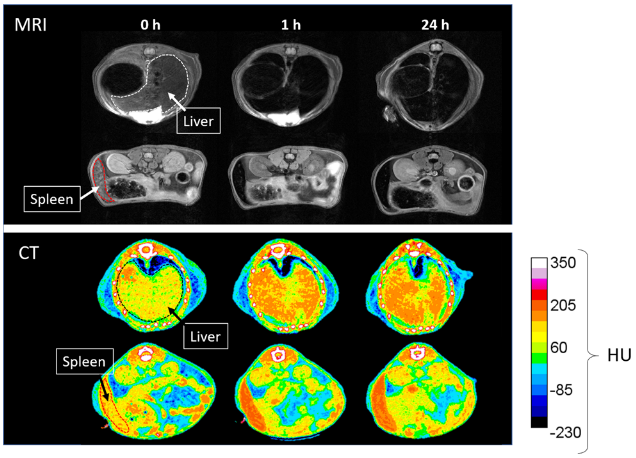

Fig. 10 Representative T_2-weighted MR images (top) and CT imaging (down) at different time points after the intravenous injection of $NaDy(WO_4)_2$ (10 mg Dy per kg animal).

appreciably after 24 h. This behavior agrees with the hepatic and splenic clearance pathways detected by HF-MRI, which is typical for nano-sized particles.[62,63] Such images also demonstrate the potential utility of $NaDy(WO_4)_2$ NPs as dual contrast agents for HF-MRI and CT bioimaging.

4. Conclusions

$NaDy(WO_4)_2$ and $NaHo(WO_4)_2$ NPs functionalized with PAA have been synthesized using a homogeneous precipitation method in polyol media at 220 °C from lanthanide nitrate and sodium tungstate precursors in a microwave oven. The NPs showed good dispersibility in water, MES, PBS and saline solution suspensions. Cell viability studies revealed that such NPs exhibited negligible toxicity effects for the human fibroblast HFF-1 cell line. Transversal relaxivity values (r_2) measured at 9.4 T were found to be higher for the $NaDy(WO_4)_2$ NPs (105.6 mM^{-1} s^{-1}) than for the $NaHo(WO_4)_2$ ones (58.6 mM^{-1} s^{-1}), which is mainly ascribed to the higher size of the former and to the higher magnetic moment of Dy^{3+} when compared with that of Ho^{3+}. Furthermore, pharmacokinetic assays carried out using tumor-bearing mice indicated that for both kinds of NPs a fast uptake by the liver and spleen took place. More importantly, certain NP accumulation in the tumor was observed 24 h after administration, indicating NPs uptake by the EPR effect, which manifests the suitability of both kinds of NPs for tumor detection through HF-MRI. On the other hand, no tissue damage was detected in the analyzed organs, which provides further support to the biocompatibility of $NaDy(WO_4)_2$ and $NaHo(WO_4)_2$ NPs. Finally, the $NaDy(WO_4)_2$ NPs, selected as a proof of concept, showed a superior X-ray attenuation capability than that of a commercial CT contrast agent (iohexol), which along with their high r_2 value make them suitable as the dual-probe for dual HF-MRI and CT imaging, as demonstrated by *in vivo* experiments conducted using healthy mice.

Author contributions

M. Ocaña: conceptualization, supervision, formal analysis, funding acquisition and writing – original draft; E. González-Gomez: methodology, data curation, formal analysis, and writing – original draft; C. Caro: data curation, formal analysis, and writing – review and editing; N. O. Nuñez: supervision and writing – review and editing; D. González-Mancebo: data curation and formal analysis; J. D. Urbano-Gámez: data curation and formal analysis; M. L. Garcia: funding acquisition, formal analysis, and writing – review and editing.

Data availability

Data for this article are available at DIGITAL CSIC at [URL – format **https://doi.org/10.20350/digitalCSIC/16522**].

Conflicts of interest

There are no conflicts to declare.

Acknowledgements

This publication is a part of the I + D + I Grants PID2021-122328OB-I00 and PID2020-118448RB-C21, funded by MCIN/AEI/10.13039/501100011033 and ''ERDF A way of making Europe''. This work was supported as well by the Junta de Andalucía under grant no. P20_00182, co-financed by EU FEDER funds. Grant PRE2019-090170 funded by the MCIN/AEI/10.13039/501100011033 and the ''ESF Investing in your future'' is also acknowledged. Relaxivity measurements were performed at the ICTS ''NANBIOSIS'', specifically in Unit 28 at the ''Instituto de Investigación Biomédica de Málaga y Plataforma en Nanomedicina (IBIMA Plataforma BIONAND)''.

References

1 H. Otsuka, *J. Med. Invest.*, 2019, **66**, 31–34.

2 R. J. Gillies and M. B. Schabath, *Cancer Epidemiol., Biomarkers Prev.*, 2020, **29**, 2556–2567.

3 E. Peng, F. H. Wang and J. M. Xue, *J. Mater. Chem. B*, 2015, **3**, 2241–2276.

4 B. Borresen, A. E. Hansen, F. P. Fliedner, J. R. Henriksen, D. R. Elema, M. Brandt-Larsen, L. K. Kristensen, A. T. Kristensen, T. L. Andresen and A. Kjaer, *Int. J. Nanomed.*, 2020, **15**, 8571–8581.

5 A. Nowogrodzki, *Nature*, 2018, **563**, 24–26.

6 T. Okada, T. Akasaka, D. H. D. Thuy and T. Isa, *Magn. Reson. Med. Sci.*, 2022, **21**, 531–537.

7 A. Gnach and A. Bednarkiewicz, *Nano Today*, 2012, **7**, 532–563.

8 M. Norek, E. Kampert, U. Zeitler and J. A. Peters, *J. Am. Chem. Soc.*, 2008, **130**, 5335–5340.

9 G. K. Das, Y. Zhang, L. D'Silva, P. Padmanabhan, B. C. Heng, J. S. C. Loo, S. T. Selvan, K. K. Bhakoo and T. T. Y. Tan, *Chem. Mater.*, 2011, **23**, 2439–2446.

10 M. Rohrer, H. Bauer, J. Mintorovitch, M. Requardt and H. J. Weinmann, *Invest. Radiol.*, 2005, **40**, 715–724.

11 I. M. Noebauer-Huhmann, P. Szomolanyi, V. Juras, O. K. Dipl, M. E. Ladd and S. Trattnig, *Invest. Radiol.*, 2010, **45**, 554–558.

12 H. Du, Q. Y. Wang, Z. Y. Liang, Q. L. Li, F. Y. Li and D. S. Ling, *Nanoscale*, 2022, **14**, 17483–17499.

13 S. Tong, S. J. Hou, Z. L. Zheng, J. Zhou and G. Bao, *Nano Lett.*, 2010, **10**, 4607–4613.

14 S. K. Wan, F. Z. Cui, B. Li, K. L. Zhao, H. N. He, Y. Zhang, J. H. Liu, L. Zhang and K. Liu, *ACS Appl. Nano Mater.*, 2020, **3**, 9433–9439.

15 H. Dong, S. R. Du, X. Y. Zheng, G. M. Lyu, L. D. Sun, L. D. Li, P. Z. Zhang, C. Zhang and C. H. Yan, *Chem. Rev.*, 2015, **115**, 10725–10815.

16 L. Helm, *Future Med. Chem.*, 2010, **2**, 385–396.

17 B. M. Alsaadi, F. J. C. Rossotti and R. J. P. Williams, *J. Chem. Soc., Dalton Trans.*, 1980, 2147–2150.

18 D. F. Jackson and D. J. Hawkes, *Phys. Rep.*, 1981, **70**, 169–233.

19 N. O. Nunez, F. Cusso, E. Cantelar, B. Martin-Gracia, J. M. de la Fuente, A. Corral, M. Balcerzyk and M. Ocana, *Nanomaterials*, 2020, **10**, 149.

20 P. A. Jarzyna, A. Gianella, T. Skajaa, G. Knudsen, L. H. Deddens, D. P. Cormode, Z. A. Fayad and W. J. M. Mulder, *Phys. Rep.*, 2010, **2**, 138–150.

21 Y. Zhang, V. Vijayaragavan, G. K. Das, K. K. Bhakoo and T. T. Y. Tan, *Eur. J. Inorg. Chem.*, 2012, 2044–2048.

22 D. Gonzalez-Mancebo, A. I. Becerro, T. C. Rojas, M. L. Garcia-Martin, J. M. de la Fuente and M. Ocana, *Part. Part. Syst. Charact.*, 2017, **34**, 1700116.

23 X. H. Zhang, B. Blasiak, A. J. Marenco, S. Trudel, B. Tomanek and F. van Veggel, *Chem. Mater.*, 2016, **28**, 3060–3072.

24 G. K. Das, N. J. J. Johnson, J. Cramen, B. Blasiak, P. Latta, B. Tomanek and F. van Veggel, *J. Phys. Chem. Lett.*, 2012, **3**, 524–529.

25 D. Lisjak, O. Plohl, J. Vidmar, B. Majaron and M. Ponikvar-Svet, *Langmuir*, 2016, **32**, 8222–8229.

26 M. I. Saleh, B. Ruhle, S. Wang, J. Radnik, Y. You and U. Resch-Genger, *Sci. Rep.*, 2020, **10**, 191318.

27 S. Guth, S. Hueser, A. Roth, G. Degen, P. Diel, K. Edlund, G. Eisenbrand, K.-H. Engel, B. Epe, T. Grune, V. Heinz, T. Henle, H.-U. Humpf, H. Jaeger, H.-G. Joost, S. E. Kulling,

A. Lampen, A. Mally, R. Marchan, D. Marko, E. Muehle, M. A. Nitsche, E. Roehrdanz, R. Stadler, C. van Thriel, S. Vieths, R. F. Vogel, E. Wascher, C. Watzl, U. Noethlings and J. G. Hengstler, *Arch. Toxicol.*, 2020, **94**, 1375–1415.

28 M. Vozlic, T. Cernic, S. Gyergyek, B. Majaron, M. Ponikvar-Svet, U. Kostiv, D. Horak and D. Lisjak, *Dalton Trans.*, 2021, **50**, 6588–6597.

29 S. Marasini, H. Yue, S. L. Ho, H. Cha, J. A. Park, K. H. Jung, A. Ghazanfari, M. Y. Ahmad, S. Liu, K. S. Chae, Y. Chang and G. H. Lee, *Bull. Korean Chem. Soc.*, 2020, **41**, 829–836.

30 S. Marasini, H. Yue, S. L. Ho, J. A. Park, S. Kim, K.-H. Jung, H. Cha, S. Liu, T. Tegafaw, M. Y. Ahmad, A. Ghazanfari, K.-S. Chae, Y. Chang and G. H. Lee, *Nanomaterials*, 2021, **11**, 11051355.

31 E. Gomez-Gonzalez, C. Caro, D. Martinez-Gutierrez, M. L. Garcia-Martin, M. Ocana and A. I. Becerro, *J. Colloid Interface Sci.*, 2021, **587**, 131–140.

32 E. Gomez-Gonzalez, C. Caro, M. L. Garcia-Martin, A. Isabel Becerro and M. Ocana, *Nanoscale*, 2022, **14**, 11461–11470.

33 E. Gomez-Gonzalez, N. O. Nunez, C. Caro, M. L. Garcia-Martin, Y. Fernandez-Afonso, J. M. de la Fuente, M. Balcerzyk and M. Ocana, *Inorg. Chem.*, 2021, **60**, 152–160.

34 E. Gómez-González, N. O. Núñez, C. Caro, M. L. García-Martín and M. Ocaña, *J. Colloid Interface Sci.*, 2023, **629**, 310–321.

35 X. P. Duan and Y. P. Li, *Small*, 2013, **9**, 1521–1532.

36 P. C. Hiemenz and R. Rajagopalan, *Principles of colloid and surface chemistry*, New York, 3rd edn, 1997.

37 D. Klee and H. Hocker, *Biomed. Appl. Polym. Blends*, 1999, **149**, 1–57.

38 P. Rivera-Gil, D. J. De Aberasturi, V. Wulf, B. Pelaz, P. Del Pino, Y. Y. Zhao, J. M. De La Fuente, I. R. De Larramendi, T. Rojo, X. J. Liang and W. J. Parak, *Acc. Chem. Res.*, 2013, **46**, 743–749.

39 M. A. Subhan, S. S. K. Yalamarty, N. Filipczak, F. Parveen and V. P. Torchilin, *J. Pers. Med.*, 2021, **11**, 571.

40 Y. Matsumura, *J. Controlled Release*, 2022, **348**, 966–969.

41 Y. Zi, K. Yang, J. He, Z. Wu, J. Liu and W. Zhang, *Adv. Drug Delivery Rev.*, 2022, **188**, 114449.

42 C. Caro and D. Pozo, *Curr. Pharm. Des.*, 2015, **21**, 4822–4836.

43 J. W. Nichols and Y. H. Bae, *J. Controlled Release*, 2014, **190**, 451–464.

44 C. Caro, A. Avasthi, J. M. Paez-Munoz, M. Pernia Leal and M. L. Garcia-Martin, *Biomater. Sci.*, 2021, **9**, 7984–7995.

45 C. Caro, C. Guzzi, I. Moral-Sanchez, J. D. Urbano-Gamez, A. M. Beltran and M. L. Garcia-Martin, *Adv. Healthcare Mater.*, 2024, 2304049.

46 E. Gomez-Gonzalez, D. Gonzalez-Mancebo, N. O. Nunez, C. Caro, M. L. Garcia-Martin, A. I. Becerro and M. Ocana, *J. Colloid Interface Sci.*, 2023, **646**, 721–731.

47 J. Edelson, D. Shaw and G. Palace, *J. Pharm. Sci.*, 1984, **73**, 993–995.

48 C. Caro, J. M. Paez-Munoz, A. M. Beltran, M. P. Leal and M. L. Garcia-Martin, *ACS Appl. Nano Mater.*, 2021, **4**, 4199–4207.

49 V. K. Lamer and R. H. Dinegar, *J. Am. Chem. Soc.*, 1950, **72**, 4847–4854.

50 M. Li, J. Wu, H. Jia, M. Wang and Z. Liu, *J. Mater. Sci.: Mater. Electron.*, 2019, **30**, 10465–10474.

51 L. J. Kirwan, P. D. Fawell and W. van Bronswijk, *Langmuir*, 2003, **19**, 5802–5807.

52 UNE-EN ISO 10993-5:2009: Evaluación biológica de productos sanitarios. Parte 5: Ensayos de citotoxicidad *in vitro*, https://www.aenor.com/.

53 S. Viswanathan, Z. Kovacs, K. N. Green, S. J. Ratnakar and A. D. Sherry, *Chem. Rev.*, 2010, **110**, 2960–3018.

54 A. Dash, B. Blasiak, B. Tomanek, P. Latta and F. C. J. M. van Veggel, *ACS Appl. Mater. Interfaces*, 2021, **13**, 24345–24355.

55 Y. L. Balachandran, W. Wang, H. Yang, H. Tong, L. Wang, F. Liu, H. Chen, K. Zhong, Y. Liu and X. Jiang, *ACS Nano*, 2022, **16**, 5647–5659.

56 K. M. Tsoi, S. A. MacParland, X.-Z. Ma, V. N. Spetzler, J. Echeverri, B. Ouyang, S. M. Fadel, E. A. Sykes, N. Goldaracena, J. M. Kaths, J. B. Conneely, B. A. Alman, M. Selzner, M. A. Ostrowski, O. A. Adeyi, A. Zilman, I. D. McGilvray and W. C. W. Chan, *Nat. Mater.*, 2016, **15**, 1212–1221.

57 A. Karageorgis, S. Dufort, L. Sancey, M. Henry, S. Hirsjaervi, C. Passirani, J.-P. Benoit, J. Gravier, I. Texier, O. Montigon, M. Benmerad, V. Siroux, E. L. Barbier and J.-L. Coll, *Sci. Rep.*, 2016, **6**, 21417.

58 G. Song, D. B. Darr, C. M. Santos, M. Ross, A. Valdivia, J. L. Jordan, B. R. Midkiff, S. Cohen, N. Nikolaishvili-Feinberg, C. R. Miller, T. K. Tarrant, A. B. Rogers, A. C. Dudley, C. M. Perou and W. C. Zamboni, *Clin. Cancer Res.*, 2014, **20**, 6083–6095.

59 S. Wilhelm, A. J. Tavares, Q. Dai, S. Ohta, J. Audet, H. F. Dvorak and W. C. W. Chan, *Nat. Rev. Mater.*, 2016, **1**, 16014.

60 P. Carrillo, M. Bernal, C. Tellez-Quijona, A. D. Marrero, I. Vidal, L. Castilla, C. Caro, A. Dominguez, M. L. Garcia-Martin, A. R. Quesada, M. A. Medina and B. Martinez-Poveda, *Biomed. Pharmacother.*, 2023, **158**, 114070.

61 D. Gonzalez Mancebo, A. Isabel Becerro, A. Corral, M. Moros, M. Balcerzyk, J. M. de la Fuente and M. Ocana, *ACS Omega*, 2019, **4**, 765–774.

62 M. Longmire, P. L. Choyke and H. Kobayashi, *Nanomedicine*, 2008, **3**, 703–717.

63 F. Alexis, E. Pridgen, L. K. Molnar and O. C. Farokhzad, *Mol. Pharmaceutics*, 2008, **5**, 505–515.